Petroleum Science 20 (2023) 3854–3864

Contents lists available at ScienceDirect

Petroleum Science

journal homepage: www.keaipublishing.com/en/journals/petroleum-science

Original Paper

MRI insight on multiphase flow in hydrate-bearing sediment and development mechanism of hydrate seal

Guo-Jun Zhao [a], Ming-Jun Yang [a], Xin Lv [b], Jia-Nan Zheng [a, c, *], Yong-Chen Song [a, **]

[a] *Key Laboratory of Ocean Energy Utilization and Energy Conservation of Ministry of Education, Dalian University of Technology, Dalian 116024, Liaoning, China*
[b] *CNOOC Research Institute Co. Ltd, Beijing, 100027, China*
[c] *Shanghai Institute for Advanced Study, Zhejiang University, Shanghai, 201203, China*

ARTICLE INFO

Article history:
Received 22 November 2022
Received in revised form
4 March 2023
Accepted 20 July 2023
Available online 21 July 2023

Edited by Jia-Jia Fei

Keywords:
Gas hydrate
Gas-water migration
Underlying gas
Hydrate seal
Pore difference
MRI

ABSTRACT

Gas and water migration through the hydrate-bearing sediment are characteristic features in marine gas hydrate reservoirs worldwide. However, there are few experimental investigations on the effect of water-gas flow on the gas hydrate reservoir. In this study, gas-water migration in gas hydrate stability zone (GHSZ) was investigated visually employing a high-resolution magnetic resonance imaging (MRI) apparatus, and the formation of hydrate seal was experimentally investigated. Results revealed that normal flow of gas-water at the low flow rate of 1–0.25 mL/min will induce the hydrate reformation. Conversely, higher gas-water flow rates (at 2–0.5 and 4–1 mL/min) need higher reservoir pressure to induce the hydrate reformation. In addition, the hydrate reformation during the gas-water flow process produced the hydrate seal, which can withstand an over 9.0 MPa overpressure. This high overpressure provides the development condition for the underlying gas and/or water reservoir. A composite MRI image of the whole hydrate seal was obtained through the MRI. The pore difference between hydrate zone and coexistence zone produces a capillary sealing effect for hydrate seal. The hydrate saturation of hydrate seal was more than 51.6%, and the water saturation was more than 19.3%. However, the hydrate seal can be broken through when the overpressure exceeded the capillary pressure of the hydrate seal, which induced the sudden drop of reservoir pressure. This study provides a scientific explanation for the existence of high-pressure underlying gas below the hydrate layer and is significant for the safe exploitation of these common typical marine hydrate reservoirs.

1. Introduction

Natural gas hydrate (NGH) is a kind of ice-like crystalline compound formed with sufficient water and gas (such as methane, and carbon dioxide) under low temperature and high-pressure conditions (Liu et al., 2016; Zhao et al., 2022b). With the increasing demand for energy sources worldwide, more and more attention has been paid to the development of NGH resources over the last few decades (Collett et al., 2015; Dong et al., 2022; Liu et al., 2019a; Makogon et al., 2007; Sadeq et al., 2018b). In natural onshore permafrost areas and offshore continental margins, methane hydrate is widely detected with the estimated global methane gas source from 10^{15} to 10^{20} m^3 (Li et al., 2016; Zhao et al., 2022a). To date, many countries have launched exploitation projects of gas hydrate for future commercial exploitation (Konno et al., 2017; Liu et al., 2019a; Wang et al., 2018). As a potential energy source, NGH has attached the attention of scholars all over the world, especially in developed countries and countries lacking conventional oil and gas sources (Sadeq et al., 2018a, b, c, 2017). The studies on the accumulation mechanism of marine gas hydrate and underlying gas are conducive to the safe and efficient exploitation of gas hydrate (Zhang et al., 2022).

Although the thermodynamic stable conditions for methane hydrate are satisfied throughout most of the ocean sediments, the distributions of gas hydrate are controlled by the availability of

---

* Corresponding author. Key Laboratory of Ocean Energy Utilization and Energy Conservation of Ministry of Education, Dalian University of Technology, Dalian, 116024, Liaoning, China.
** Corresponding author.
E-mail addresses: zhengjn@dlut.edu.cn, zhengjn@zju.edu.cn (J.-N. Zheng), songyc@dlut.edu.cn (Y.-C. Song).

https://doi.org/10.1016/j.petsci.2023.07.017

methane gas (Davie and Buffett, 2003). The methane supply of gas hydrate in marine sediments is commonly attributed to the local conversion of organic material within hydrate stability zone or migration of methane-containing fluids from deeper zone (Davie and Buffett, 2003; Pohlman et al., 2009). The origin of the methane in formed hydrate is predominantly biogenic or thermogenic, or a combination of both (Xu and Ruppel, 1999). NGHs generally coexist with free gas or/and free water (Kannberg et al., 2013). Thus, the hydrate reservoirs are generally divided into four classes based on the difference in coexistence (Li et al., 2016). Class 1 is the hydrate-bearing sediment that covers the two-phase fluid zone (with water and free gas). The hydrate saturation of hydrate-bearing sediment is high enough, which produces a relatively low effective permeability zone for underlying free gas and water zone (De La Fuente et al., 2021). Class 2 is that hydrate-bearing sediment covers a mobile water layer, such as hydrate reservoirs in Eastern Nankai Trough and Mallik sites (Huang et al., 2009; Yu et al., 2019). Class 3 is that only a hydrate-bearing sediment layer exists. Besides, class 4 hydrate reservoirs are unconfined geological strata with low hydrate saturation, which usually appear as nodules (Moridis et al., 2009). The class 1 reservoir is the most potent type for commercial exploitation of hydrate, which is highly significant for investigation (Zhao et al., 2022c).

Gaseous methane and water migration through the hydrate stability zone are characteristic features in geological settings along tectonically active and passive continental margins (Kannberg et al., 2013; Liu et al., 2019b; Smith et al., 2014). The underlying gas beneath the hydrate layer is developed by the continual gas migration from deeper layer (You et al., 2015). In other words, the overlying hydrate-bearing sediments produce a sealing effect on the underlying gas and water, which is the capillary seals (Cathles, 2007). The mechanism of the sealing effect for the gas hydrate layer is the capillary force between water and hydrate (Su et al., 2009). Early in 1999, Clennell et al. (1999) analyzed the effect of capillary pressure on pore pressure systematically. They found that the gas pressure below the hydrate layer was higher than the theoretical pressure, which was caused by the capillary pressure. In recent years, the research of gas hydrates has been gradually developing in the microscopic direction, and the influence of capillary force on gas hydrate has been paid more attention. Touil et al. (2019) studied the formation of carbon dioxide hydrate in a thin glass tube, the capillary force constrained the direction of hydrate growth, and hydrate growth along the front of the glass wall. Buleiko et al. (2017) studied the changes of propane hydrate formation pressure in porous media using a microcalorimeter. The thermodynamic properties of propane were changed by the capillary effect of pores, which affected the formation of propane hydrate.

When the gas accumulates beneath the hydrate-bearing sediments until the gas pressure exceeds the least principal stress in the overlying hydrate zone, hydraulic fractures form, gas and water are vented to the surface and form the clod vent (Meazell and Flemings, 2022). The appearance of the cold vent is a typical breakthrough of hydrate-containing sealing layer (Bünz et al., 2003). The gas and seawater generated by the breakthrough of hydrate-bearing sealing layer will lead to the sedimentary layer deformation above the hydrate layer, which may cause the marine geological disaster (Yang et al., 2020). Therefore, the destruction of hydrate-containing sealing layer must be considered during the hydrate exploitation process.

Either the formation of hydrate reservoirs or artificial hydrate exploitation in marine sediments is accompanied by gas and/or water flow (Yuan et al., 2017). In recent years, there were simulation studies and experimental studies on the effect of gas-water migration and hydrate formation. Chatterjee et al. (2014) simulated the hydrate and free gas accumulation in heterogeneous marine sediment through a two-dimensional numerical model. Kang et al. (2021) simulate the multiphase flow of hydrate slurry in the annulus by combining the hydrate dissociation kinetic model with the established annulus hydrate slurry multiphase flow model. They found that larger flow rate of multiphase induced smaller length of the slug flow. Behseresht and Bryant (2017) studied the physical mechanisms between gas and water flow associated with hydrate formation using a transient 1-D transport model. They found that not only the petrophysical propertied of the host sediment, but also the hydrate formation rate and temperature cooling rate had a decisive impact on hydrate saturation profiles. Seol and Kneafsey (2011) performed a numerical study studied on the effects of pore space hydrate formation habits on water and gas migration. When the hydrate saturation exceeded 40%, the absolute permeability in hydrate-bearing sediment sample decreased significantly with the increases of hydrate saturation. In addition, complete plugging of gas and water flow occurred when hydrate saturation approached 70%. Yang et al. (2019) investigated the promoting effect of gas-water migration on hydrate dissociation using MRI. Chen et al. (2020) studied the water-gas migration process using MRI system, they found that water flow can induce the hydrate dissociation, and hydrate-bearing sediment with lower hydrate saturation could benefit more from water flow.

The researches on the effect of gas-water migration and hydrate formation mainly focused on simulation studies. The experimental researches mainly focused on the promoting effect of gas-water migration on hydrate exploitation. In addition, the MRI technique was widely used in the investigations on gas and water flow in hydrate-bearing sediments, because it can distinguish solid hydrate and liquid water (Song et al., 2015; Yang et al., 2022). In this study, the effect of gas-water flow on the formation of hydrate seal were firstly experimentally investigated using MRI technique. The research considerations were quite novel, and the results had practical application values for understanding the characteristics of hydrate reservoirs and they were significant for guiding hydrate safe exploitation.

2. Experimental apparatus and procedure

2.1. Apparatus

Fig. 1 demonstrates the schematic experimental apparatus in this study. The core device was the MRI system, which was manufactured by Varian, Inc Palo Alto, CA, USA. The magnetic field strength of MRI was 9.4 T and it was operated at 400 MHz. The two-dimensional MRI images were constructed using a standard spin echo multi-slice pulse sequence (Wang et al., 2017). The echo time (TE) was 4.39 ms, and the repetition time (TR) was 1000 ms in this study. The field of view (FOV) was 30 mm × 30 mm with 2.0 mm thickness. In addition, the image data matrix was 128 × 128. The sequence acquisition time was 2.14 min for per MRI image in these settings. The reactor used in this work was a high-pressure polyimide tube with an effective height of 200 mm and a diameter of 15 mm. The maximum pressure limitation of the reactor was 13.0 MPa. The reactor was surrounded by a heat preservation jacket in which the coolant circulated continually to keep the tube at the required temperature.

Three high-precision ISCO pumps, which were manufactured by Teledyne ISCO Inc, Lincoln, NE, USA, were used to drive gas flow, drive water flow, and control the back pressure, respectively. The reservoir pressure was controlled the by the back pressure. Thus, the reservoir pressure and back pressure were equal. In addition, the reactor inlet was connected with the gas injection pump and water injection pump, thus, the gas pressure, the water pressure and the inlet pressure were equal. One thermostatic bath (FL300,

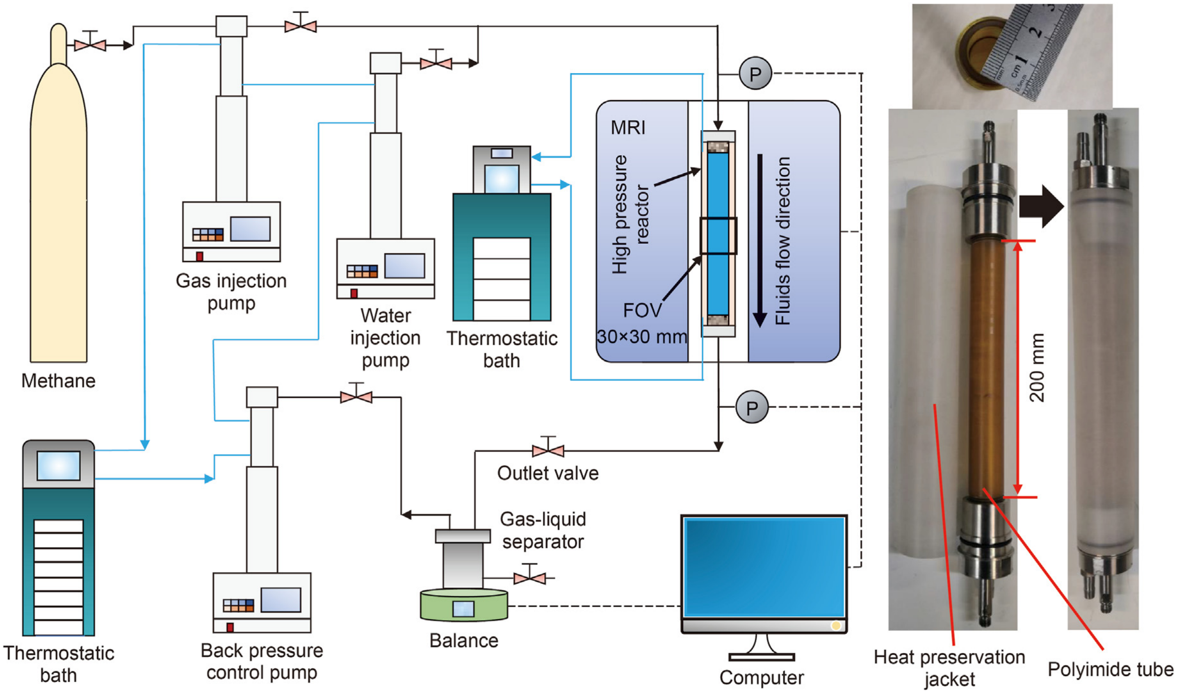

Fig. 1. Schematic of the MRI apparatus.

JULABO, Seelbach, Germany) was used to control the temperature of the reactor, and another thermostatic bath (FL 25, JULABO, Seelbach, Germany) was used to control the temperature of high-precision pumps. The pressure sensors (3510 CF, Emerson Electric Co., Ltd., St. Louis, USA) were used to measure the inlet and outlet pressure with an accuracy of ±0.05%. The outlet pressure, reservoir pressure and back pressure were equal.

The glass beads (BZ02) produced by As-One Co., Ltd., Japan were used to simulate the porous media of marine environment. The porosity of the glass beads was 35.4% (Yang et al., 2011), and the diameter of glass beads was 0.177–0.250 mm (mean particle size = 0.1 mm) (Zhang et al., 2020). In hydrate formation process, the pore water used in the reactor was deionized water. During the gas-water flow process, the sodium chloride solution with a mass fraction of 3.5% was used to configure the seawater. The methane gas with a purity of 99.99% used in the experiments was produced by Dalian Special Gases Company.

2.2. Procedures

Hydrate sample was made through sand filling, vacuum pumping, water saturation, water displacement, and pressurization. Firstly, the dried glass beads were compacted into the reactor and checked the system tightness. Secondly, the seawater was driven into the reactor by the water injection pump until the pressure approached 6.0 MPa. This was the water saturation process, which was maintained for about 30 min. The purpose of this step is to obtain the mean intensity (MI) value of water saturation state. Thirdly, closed the valve between water injection pump and reactor, then, opening the valve of the reactor outlet to make the reservoir pressure drop into the atmosphere pressure. Fourthly, displaced partial water in reactor using the gas injection pump, which ensured the initial water saturation was around 39%. The water distribution after the displacement was not completely evenly distributed, but it had no effect on the distribution of hydrate formation. The pressure of the gas injection pump is 2.5 MPa during this time. Finally, closed the reactor outlet valve and maintained the pressure at 6.0 MPa through methane injection. the hydrate formation process began at the point that the reservoir pressure reached 6.0 MPa. The real-time hydrate saturation (S_h) can be calculated by the MI value of the MRI images through the following equations (Zhang et al., 2020):

$$S_h = 1.25 \times \frac{(I_0 - I_i)}{I_0} \times S_{w0} \times 100\% \tag{1}$$

$$S_{w0} = \frac{I_0}{I_{full}} \tag{2}$$

where I_0, I_{full} and I_i are MI values of initial water saturation, complete water saturation, and water saturation at time i, respectively. S_{w0} represents the initial water saturation and can be calculated by Eq. (2). In addition, the water saturation at time i (S_{wi}) can be calculated as follow:

$$S_{wi} = \frac{I_i}{I_{full}} \tag{3}$$

Table 1 summarizes the conditions and results of hydrate-bearing samples in all Cases. It was obvious that all experimental conditions were inside the hydrate thermodynamic stable condition (274.15 K, 2.98 MPa) (Yang et al., 2022). The hydrate saturation in the marine sediments was usually considerably high, according to the geological exploration results. The average gas hydrate

Table 1
Conditions and results of hydrate-bearing samples in all cases.

Case	1	2	3	4	5	6	7
Hydrate saturation, %	35.8	36.9	34.7	34.8	34.3	35.4	34.6
Water saturation, %	49.2	50.8	52.8	49.8	57.3	54.9	55.8
Pressure, MPa	6.0						
Temperature, K	274.15						

saturation in the Krishna-Godavari basin obtained from resistivity log data and P-wave velocity modelling are 25% and 60% (Lpa et al., 2019). In addition, the gas layer existed beneath the hydrate layer in the Shenhu Area of the South China Sea, and the hydrate saturation in gas hydrate layer was 0–54.5% (31% av.) according to the results from the core analysis of SHSC-4 (Qin et al., 2020). Thus, the objective hydrate saturation of hydrate sample in this study was 35%. When the hydrate saturation reached this value, reduced the reservoir pressure to around the phase equilibrium pressure (3.5 or 4.0 MPa). Moreover, the hydrate reservoir was usually in the state of water saturation (Almenningen et al., 2018; Chong et al., 2017). Therefore, to better simulate the academician state of hydrate in the marine environment, the seawater was injected into the reactor using high-precision water injection pump at the flow rate of 0.5 mL/min. The water-saturated hydrate samples was shown in Fig. S1 in the Supporting Information. The seawater flow rate was low enough that it can be considered that there was no hydrate decomposition during this process (Sun et al., 2020b). After that, the gas and seawater were injected into the reactor at the same time.

3. Results and discussion

The characteristics of the hydrate reservoir state during the gas-water flow process were investigated using MRI visualization technology. In addition, permeability is a crucial factor to describe multiphase seepage characteristics of hydrate sediments. The reservoir permeability can be calculated by Darcy's law (Hou et al., 2018):

$$Q = K\frac{A \cdot \Delta P}{\mu \cdot L} \tag{4}$$

$$K_{\mathrm{rw}} = \frac{K(S_{\mathrm{h}})}{K} \tag{5}$$

where K is the absolute permeability, m^2; $K(S_h)$ is the effective permeability, m^2; K_{rw} is the relative permeability to water; Q is the fluid flow rate, m^3/s; A is the cross-section area that is perpendicular to the flow direction m^2; ΔP is the pressure difference applied across the sample, Pa; μ is the dynamic viscosity of the flowing fluid, P·s; L is the length of the sample, m. In this study, the hydrate saturation of the hydrate sample was around 35%, it was approached to pore-filling models (Peng et al., 2019). Thus, the permeability model, which was improved by Kleinberg et al. (2003) was used to calculate the relative permeability of the hydrate-bearing sediment, as shown in Eq. (6):

$$K_{\mathrm{rw}} = \frac{K(S_{\mathrm{h}})}{\mathrm{K}} = 1 - S_{\mathrm{h}}^2 + \frac{2(1 - S_{\mathrm{h}})^2}{\ln S_{\mathrm{h}}} \tag{6}$$

3.1. Methane-containing fluid flow characteristics in hydrate-bearing sediments

Free gas and water migration through the hydrate stability zone is a common phenomenon, which occurs either in hydrate exploitation process or hydrate accumulation stage (Shen et al., 2018). Water-gas flow at three different rates through water-saturated hydrate zone was investigated. The flow conditions of Cases 1–3 are summarized in Table 2. In Case 1, the methane gas and seawater migrated through the hydrate-bearing sediments at the flow rate of 4–1 mL/min. The hydrate saturation is positively correlated with the effective porosity and absolute permeability of the sediments, which causes the flow rate of gas and water larger than the seepage velocity of hydrate-bearing sediments. Thus, the overpressure (referred to the pressure difference between the inlet pressure and outlet pressure) appeared before 52 min, as shown in Fig. 2. In other words, the hydrate-bearing sediments with high hydrate saturation (35.8%) impeded the gas-water flow by the capillary force between the hydrate phase and water phase. After 52 min, the overpressure decreased to 0 MPa, indicating that the capillary sealing effect of the hydrate-bearing sediment disappeared. The outlet flow was the seawater volume that flowed out of reactor during the gas-water flow process, which could be regarded as a symbol to verify the existence of the capillary seals. When the sediment has the sealing effect, the seawater flow will be blocked; conversely, the seawater flows through the sediment, and the outlet flow increase. The gas-water flowed through the sediment smoothly and the overpressure decreased to 0 indicating that the gas and water migration cannot be accumulated beneath the hydrate-bearing sediment at the gas-water flow rate of 4–1 mL/min.

Different from Case 1, the overpressure continuously increased to 6.5 MPa before 163 min. The outflow tended to be constant between 90 and 163 min, indicating that the hydrate-bearing sediment showed the capillary sealing for the gas and water during this period. In addition, the overpressure increased indicating that the water and gas accumulated beneath the hydrate-bearing sediment. However, the overpressure decreased rapidly at 163 and 194 min, respectively. In addition, partial water flowed out of the reactor, indicating that the capillary seal was broken through at 163 and

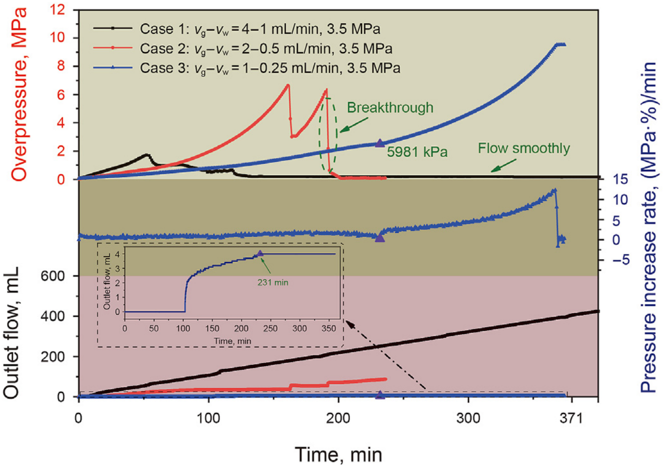

Fig. 2. Characteristics of hydrate-bearing sediment during gas-water flow process in Cases 1–3.

Table 2
Experimental conditions and results of Cases 1–3.

Case	Fluid flow conditions	Maximum overpressure, MPa	Hydrate change	Final flow state
1	4 mL/min seawater & 1 mL/min methane	1.76	Dissociation	Flow through
2	2 mL/min seawater & 0.5 mL/min methane	6.68	Reformation and dissociation	Hindrance is broken through
3	1 mL/min seawater & 0.25 mL/min methane	9.50	Reformation	Hindered

194 min. After 194 min, the overpressure turned to 0, indicating that the capillary sealing effect failed, and the free gas and water flowed through the hydrae-bearing sediments smoothly at the flow rate of 2–0.5 mL/min.

In Case 3, the gas-water flow rate was 1–0.25 mL/min. The overpressure kept increasing, which was caused by the gas and water accumulation, as shown in Fig. 2. However, the seawater continuously flowed out of the reactor before 231 min, indicating that the hydrate-bearing sediment has limited hindrance to the gas-water flow. In addition, the overpressure increase rate at *i* min can be calculated by Eq. (7):

$$R_i = \frac{P_i - P_{i+\Delta t}}{t} \cdot \% \tag{7}$$

The curve of pressure increased rate showed a stable trend before 231 min, for the reason that partial water and gas flowed through the hydrate-bearing sediment. The outflow maintained constant after this point, which indicated the hydrate-bearing sediment showed a capillary sealing effect on the external fluids after 231 min. In addition, an obvious fluctuation appeared at 231 min, which could be a symbol of the formal formation of hydrate seal. The pressure increase rate increased after 231 min, for the reason that no gas or water can flow through the hydrate-earing sediment. The overpressure increased to 9.5 MPa in the end.

The reservoir condition could be visually observed by MRI because the MRI can only acquire images of the ^{1}H contained in liquid water (Wang et al., 2020). Fig. 3(a) demonstrates the characteristics of water distributions in FOV, and Fig. 3(b) reflects the real-time characteristics of water saturation and hydrate saturation in hydrate-bearing sediments. Capillary pressure was defined by the van Genuchten model with capillary pressure (P_c) as a function of water saturation (S_w), with no hysteresis considered (Vangenuchten, 1980):

$$P_c = -P_0 \left[(S^*)^{1/\lambda} \right]^{1-\lambda} \tag{8}$$

where P_0 was the capillary entry pressure.

$$S^* = \frac{S_w - S_{irw}}{S_{mxw} - S_{irw}} \tag{9}$$

where S_{irw} represented the residual water saturation, S_{mxw} represented the max water saturation. The values of these parameters are fitting parameters except P_c and S_w. $P_0 = 0.007$ MPa, $\lambda = 4$ in this work. As the formation of hydrates, capillary pressure can be calculated using the Leverett model (Bello-Palacios et al., 2022):

$$P_c^* = P_c \sqrt{\frac{k_0}{k} \cdot \frac{\varphi}{\varphi_0}} \tag{10}$$

where φ was the hydrate-filled porosity, φ_0 was the hydrate-free porosity. $\varphi = \varphi_0(1 - S_h)$. In addition, $\frac{k}{k_0} = (1 - S_h)^N$, the magnitude of N can vary from $N = 1.25$ for sediments with uniform cementing hydrate to $N = 25$ for sediments with uniform pore-filling hydrate. Thus, the capillary pressure of the hydrate-bearing sediment can be calculated. When the gas-water flow rate was 4–1 mL/min (Case 1), the capillary pressure was 1.98 MPa. The gas and water migration were hindered by the capillary pressure, which caused the pressure to increase before 52 min. After 52 min, hydrate dissociation occurred, which caused the decrease in hydrate saturation and the increase in water saturation. In addition,

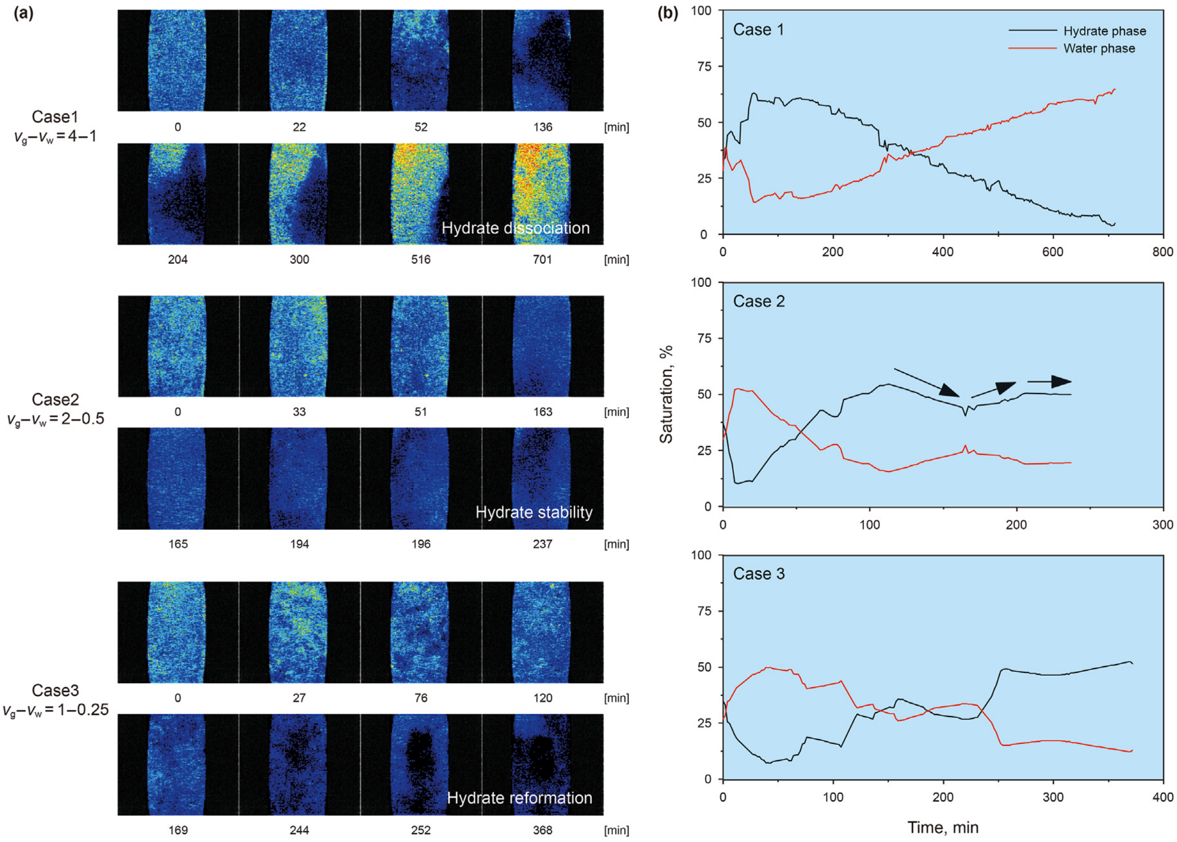

Fig. 3. Micro-images during the gas-water flow process in Cases 1–3: (**a**) MRI images; (**b**) phase saturation.

the gas and water phase flowed through the hydrate-bearing sediment after 52 min, indicating that capillary sealing effect disappeared gradually during the hydrate dissociation process. Meanwhile, the reservoir condition (274.15 K, 3.5 MPa) was in hydrate thermodynamic stable area, and the driving force for hydrate dissociation was the chemical potential difference between seawater phase and hydrate phase, which has been experimentally confirmed by Chen et al. (2019). The chemical potential difference is caused by the inadequate dissolution of methane gas in seawater (Nakayama et al., 2013; Sun et al., 2020a).

For Case 2, the changes in overpressure were positively correlated to the changes in hydrate saturation. The hydrate reformation before 120 min produced the capillary sealing to the gas-water migration. The hydrate saturation was 44.5%, and the water saturation was 24.2% at 165 min. Thus, the calculated capillary pressure was 5.91 MPa. While the overpressure was 6.68 MPa at this point, as shown in Fig. 4. The overpressure exceeded the capillary pressure and caused a sudden drop in reservoir pressure. The heterogeneity of hydrate distribution was the reason that caused the inaccurate calculation of the capillary pressure. The capillary pressure at the beginning of the overpressure plunge in the experiment was the exact capillary pressure at the moment of the breakthrough. At 195 min, the overpressure exceeded the calculated capillary pressure (6.11 MPa), which caused the pressure drop. After 196 min, the hydrate seal was absolutely broken through, and the hydrate saturation maintained stable. The breakthrough of hydrate-bearing sediment occurred at the condition that the hydrate saturation was stale. For Case 3, The MRI images darkened gradually, which indicated the hydrate reformed at the gas-water flow process. The water saturation decreased and the hydrate saturation increased during this period, indicating that hydrate formation consumed partial pore water in hydrate thermodynamic stability condition. According to the Young-Laplace equation (Kagan and Pinczewski, 2000):

$$\Delta P_{\mathrm{c}} = 2\gamma(1/r_1 - 1/r_2) \tag{11}$$

where ΔP_{c} represents the capillary pressure between the non-wetting and wetting fluids of porous medium; γ represents the interfacial tension; r_1 and r_2 represents the effective pore radius of small and large pores, respectively. The hydrate formation further reduced the effective pore radius, the water in the narrow pore space produced a larger capillary pressure, which was directed to the gas phase. At 231 min, the calculated capillary pressure was 8.76 MPa. Hydrate seal formal formed at the point that the water flow was stopped. The water and gas accumulation due to the capillary pressure and induced the overpressure increase.

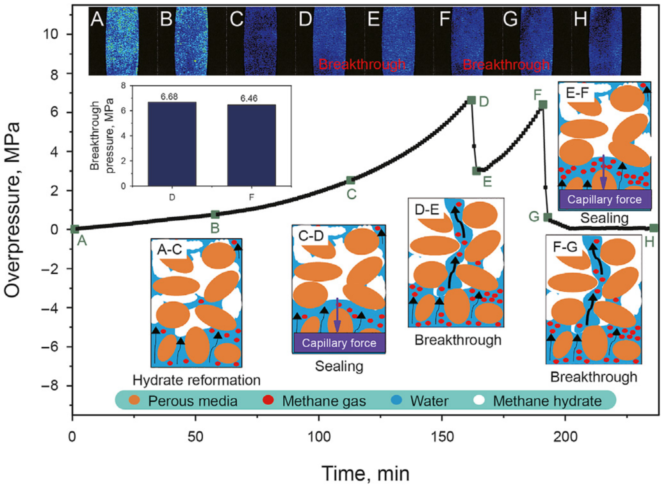

Fig. 4. Breakthrough of hydrate seal at the gas-water flow rate of 2–0.5 mL/min.

Comprehensive comparison, the gas-water flow rate was an important factor that affected the hydrate reformation and hydrate dissociation. Hydrate formed at the gas-water flow rate of 1–0.25 mL/min, for the reason that the water contacted fully with the methane gas at a lower gas-water flow rate, and the methane concentration exceeded the methane solubility. On the contrary, the methane concentration was lower than the methane solubility at high gas-water flow rate (4–1 mL/min), which caused the chemical potential difference between hydrate phase and water phase and induced the hydrate dissociation. The water and gas flow smoothly through the hydrate-bearing sediment at the hydrate dissociation process. In addition, hydrate reformation was the immediate cause for the formation of hydrate seal. The hydrate formation occupied the pore space and reduced the pore volume. The pore water was preferentially adsorbed at the smaller throat and the capillary pressure generated at the throat of the pore with small pore size, which inhibited the flow of gas and water in the pore space. The capillary sealing effect of hydrate-bearing sediment provides the development condition for higher-pressure gas reservoir under hydrate layer. However, when the hydrate saturation was in the dynamic equilibrium state (at the gas-water flow rate of 2–0.5 mL/min), the hydrate seal can be broken through by enough overpressure. The breakthrough pressure was the overpressure at the point that pressure started to drop. There was a pressure sudden drop in reservoir pressure, which may cause geological disasters. Thus, the overpressure caused by the gas-water flow has to be taken seriously, which will produce an adverse effect on hydrate exploitation.

3.2. *Sealing characteristics of the hydrate-bearing reservoir on external fluids*

Gas hydrate not only occurred in the region near the thermodynamic stability condition of hydrate, but also the region above the thermodynamic stability condition (Riedel and Collett, 2017). The gas-water flow at higher pressure condition (4.0 MPa) was investigated at the flow rate of 2–0.5 and 4–1 mL/min. The experimental conditions of Cases 4 and 5 are summarized in Table 3. Taking the injection volume as the reference value, it was found that high flow rate (Case 5) has a hysteresis phenomenon compared with low flow rate (Case 4), but the higher flow rate consumed less time.

As shown in Fig. 5, the overpressure increased with the gas-water flow, and the outflow was maintained stable at 94 and 54 min in Cases 4 and 5, respectively, which indicated the formal formation of hydrate seal. The gas-water flow rate of Case 2 was the same as it was in Case 4, and the gas-water flow rate of Case 1 was the same as it was in Case 5. The hydrate seal formed in Cases 4 and 5 indicated that the gas-water flow in the higher-pressure zone was more conductive to the formation of hydrate seal. Because higher pressure provides the larger driving force for hydrate formation by enhancing the mass transfer between the gas and water (Ma et al., 2020). Moreover, the curve of pressure increases rate fluctuated at the beginning point of hydrate seal formally formed, which also appeared in Case 3. This fluctuation of pressure increase can be regarded as a marker to judge the formation of the hydrate seal.

Fig. 6 demonstrates the variation characteristics of hydrate saturation in FOV during the gas-water flow process of Cases 4 and 5. The MRI images darkened in Case 5 and hydrate saturation increased during the gas-water flow process. The increase in hydrate saturation produced the hydrate seal at 52 min. The water saturation increased after 72 min, which was caused by the gas and

Table 3
Experimental conditions and results of Cases 4 and 5.

Case	Fluid flow conditions	Maximum overpressure, MPa	Hydrate change	Final flow state
4	2 mL/min seawater & 0.5 mL/min methane	9.00	Reformation	Hindered at 94 min
5	4 mL/min seawater & 1 mL/min methane	9.00	Reformation	Hindered at 54 min

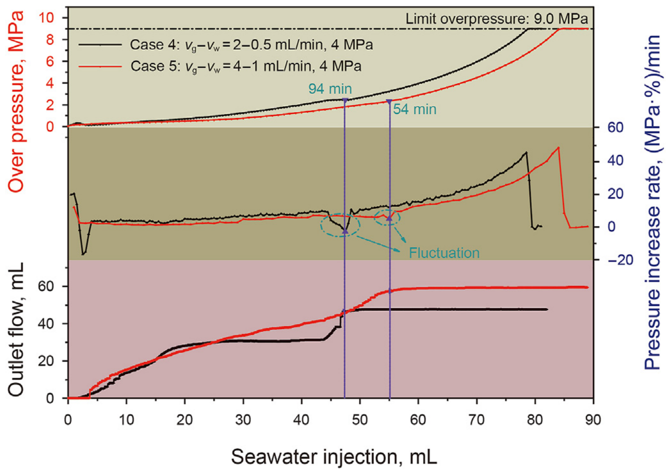

Fig. 5. Characteristics of hydrate-bearing sediment during gas-water flow process in Cases 4 and 5.

water migration above the hydrate sealing zone. In other words, the hydrate sealing zone was below the FOV. In Case 4, the hydrate saturation did not show an increasing trend under the condition that the hydrate seal formed during the gas-water flow process. However, it was found that there was a significant change in the lower-left corner of FOV in Case 4. Thus, the changes in the MI value of Line 1 at different times were shown in Fig. S2 in the Supporting information. The MI value between 0–4.2 mm was decreasing, indicating that hydrate formed in this area and consumed the pore water. Thus, the hydrate was estimated to be formed outside the FOV, and it was imperative to obtain the full MRI images of reactor, which was beneficial for investigating the hydrate seal comprehensively.

The multi-level MRI image (4 layers) was carried out by adjusting the position of the reactor. The camera on the MRI device remained stationary and moved the reactor 30 mm upwards after each shot, a complete reservoir state was presented by this operation. Fig. 7 demonstrates the multi-level MRI images of the hydrate reservoir after the overpressure reached 9.0 MPa. In addition, the MRI images in other figures was in the position 1, as shown in Fig. 7(a). A significant boundary of remaining water after hydrate reformation could be found in the hydrate reservoir, which was the interface of hydrate zone and coexistence zone (consisting of hydrates, free gas, and seawater). The hydrate saturation increased along with the gas-water migration direction, which even reached 94.7% in area C, as shown in Fig. 7(b). Thus, the gas-water flow was a feasible method to produce hydrate-bearing sediment with high hydrate saturation, either at the high-pressure condition (4.0 MPa, 274.15 K, 2–0.5 mL/min) or at low flow rate condition (1–0.25 mL/min, 3.5 MPa, 574.15 K). The water, hydrate, and gas coexisted in areas A and B, which were defined as coexistence zones. The

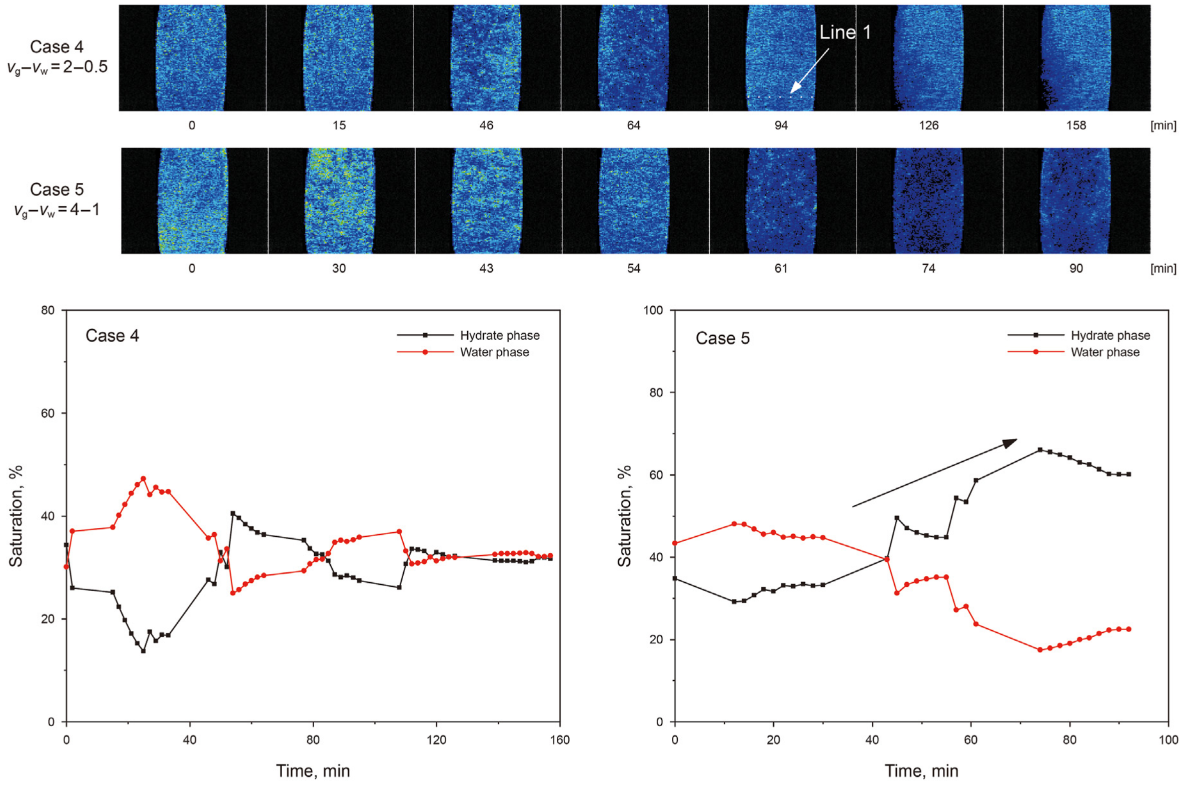

Fig. 6. Hydrate and water distribution during gas-water flow process in Cases 4 and 5.

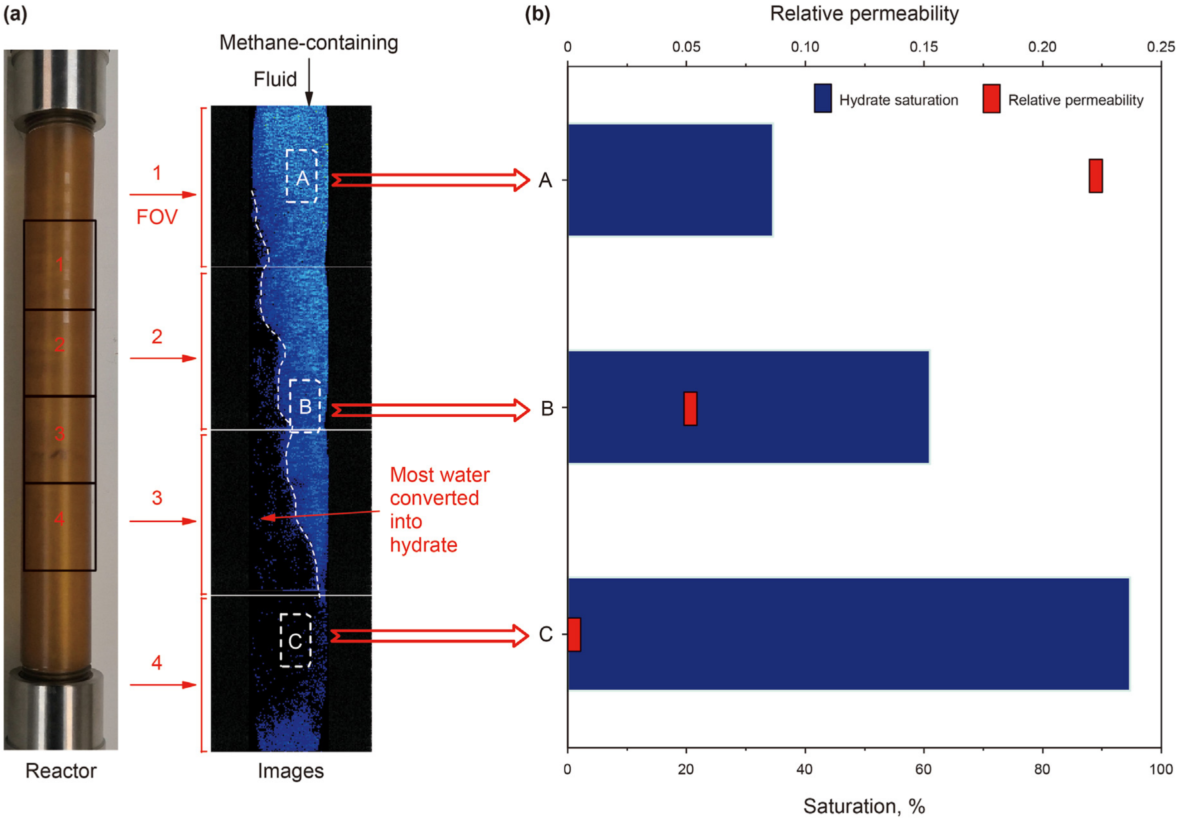

Fig. 7. Analysis of hydrate distribution of hydrate seal in Case 4: (**a**) multi-level MRI images; (**b**) hydrate saturation and relative permeability in different areas.

capillary pressure generated at the area near the interface was caused by the pore difference between hydrate zone and coexistence zone. The hydrate-bearing sediment showed a capillary sealing effect on the flow of the external fluid. Thus, the gas and water accumulated above the hydrate seal, which led to high overpressure. This hydrate-bearing sediment of Case 4 was similar to the hydrate reservoir in the South China Sea (Qin et al., 2020), in which the hydrate layer, coexistence layer, and free gas layer were vertically distributed. The experimental phenomenon is consistent with the model for free gas migration presented by Liu and Flemings (2006). The hydrate reservoir in marine sediments with underlying gas and/or water layer was most likely accumulated through the gas-water flow.

Fig. 8 demonstrates the characteristics of the formation hydrate seal. Comprehensive comparison, high pressure was conducive to inducing the formation of hydrate seal, as shown in Fig. 8(a). Significantly, the overpressure reached 9.0 MPa at the constant back pressure of 4.0 MPa. It should be emphasized that the limit pressure is 13.0 MPa in this study, which was limited by the experimental apparatus. The overpressure may be higher than 9.0 in practice. More importantly, this overpressure was caused by the gas and water accumulation, which provided development condition of high-pressure gas layer beneath the hydrate layer. In addition, gas-water flow rates affected the formation time of hydrate seal. As shown in Fig. 8(b), higher gas-water flow rate was more conducive to the formation of hydrate seal under the same gas-water flow rate ratio.

3.3. *Effects of fluids flow with variable flow rate on the formation of hydrate seal*

The flow rate of fluids flow in hydrate-bearing sediment was variable, and was influenced by the geological formations, temperature, pressure, and so on (Yang et al., 2018). The fluids flow with variable flow rate was investigated by changing the gas-water injection rate, and the experimental conditions of Cases 6 and 7 are summarized in Table 4. The gas-water process was divided into two stages: in the first stage the gas-water flow rate was 1–2 mL/min, in the second stage, the gas-water flow rate was 2–0.5 mL/min in Case 6 and 4–1 mL/min in Case 7, respectively, and the diagram was shown in Fig. S3 in the Supporting Information.

Fig. 9 demonstrates the characteristics of reservoir state during variable gas-water flow process. In stage 1 (S_1), the overpressure was 0.2 MPa and the gas and water flowed through the reservoir smoothly, indicating the hydrate-bearing sediment cannot accumulate the gas and water. In addition, the MRI images of S_1 brightened, which indicated that water flow through the reactor. The hydrate saturation decreased at the gas-water flow rate of 1–2 mL/min, for the reason that the methane was unsaturated, which induced the mass transfer between hydrate phase and seawater phase driven by the chemical potential difference between hydrate and water. The random distribution of hydrate in porous media was the reason that the water distribution in Case 6 at 146 min was different from that in Case 7 (Zhang et al., 2019). The hydrate seal cannot form during the hydrate dissociation process, which was constant with the result in Case 1.

In stage 2 (S_2), the flow rate ratio of gas-water converted from 1 to 2 to 4–1. The hydrate saturation increased at S_2, as shown in Fig. 9(b). The hydrate seal formed at 246 min in Case 6 and 202 min in Case 7, respectively, which further proved that high gas-water flow rate was conducive to the formation of hydrate seal. In addition, the overpressure fluctuated after the formation of hydrate seal, which occurred at 274 min in Case 6 and 227 min in Case 7. The water migrated in the area where the hydrate dissociated in S_1, for

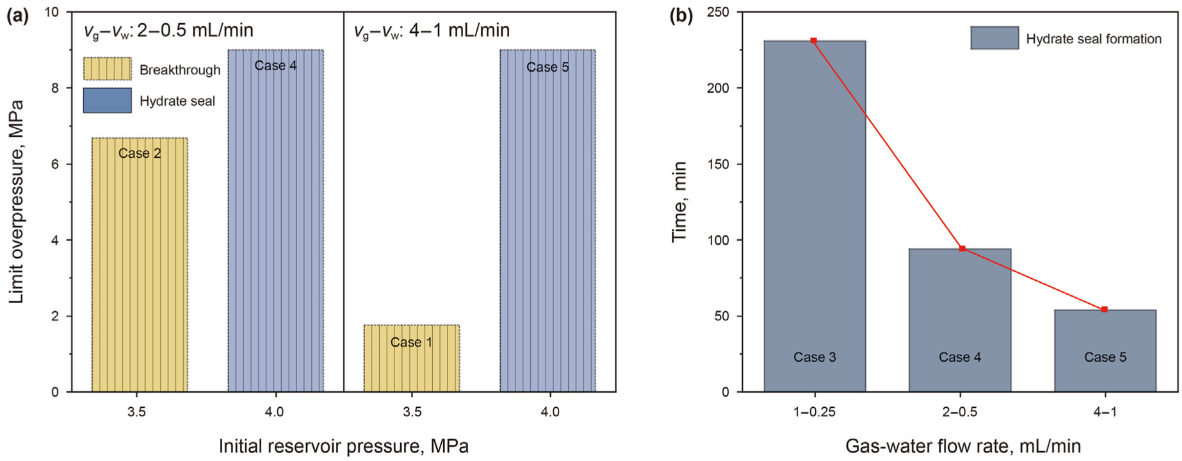

Fig. 8. Characteristics of the formation of hydrate seal: (**a**) influence of pressure; (**b**) influence of flow rates.

Table 4
Experimental conditions and results of Cases 6 and 7.

Case	Fluid flow conditions in step 1	Fluid flow conditions in step 2	Hydrate change	Final flow state
6	1 mL/min seawater & 2 mL/min methane	2 mL/min seawater & 0.5 mL/min methane	Dissociation in step 1 and reformation in step 2	Hindered at 246 min
7	1 mL/min seawater & 2 mL/min methane	4 mL/min seawater & 1 mL/min methane	Dissociation in step 1 and reformation in step 2	Hindered at 202 min

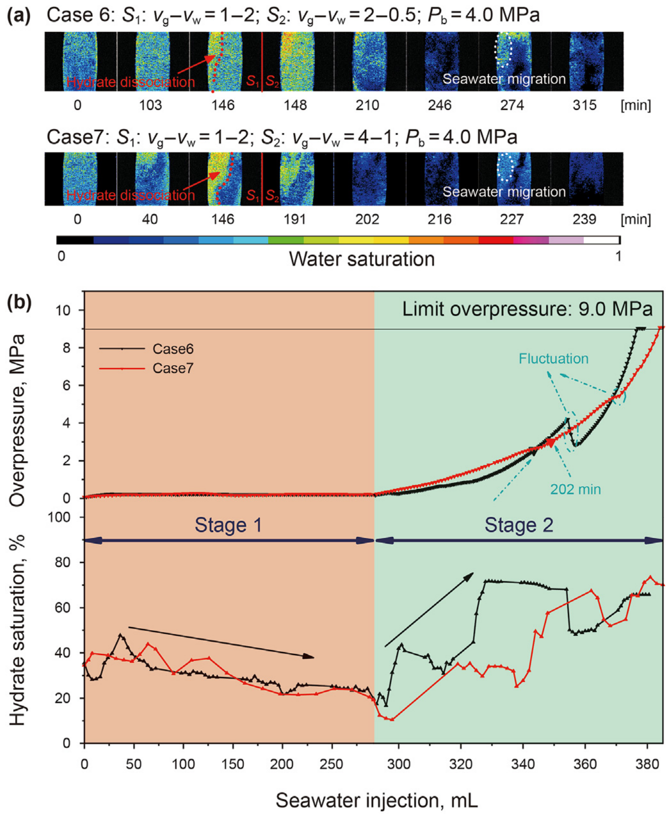

Fig. 9. Characteristics of reservoir state during variable gas-water flow process: (**a**) MRI images; (**b**) overpressure and hydrate saturation.

the reason that the hydrate saturation was lower in these areas. The gas and/or water with overpressure can be punctured into the area, where the hydrate has been dissociated by unsaturated water. This may be the reason that induced the clod vents in marine sediments, and the hydrate dissociation areas tended to form the chimney in the hydrate reservoir (Torres et al., 2004).

The hydrate seal formed in Cases 3, 4, 5, 6, and 7, and the overpressure reached at least 9.0 MPa. The distribution of water and hydrate in hydrate seal could be reflected through MRI images. It could be seen from Fig. 7, the obvious interface of hydrate zone and coexistence zone existed in the hydrate seal in Case 4. Hydrate reformation changes the reservoir structure, which caused the pore difference in hydrate zone and coexistence zone. The hydrate saturation in hydrate zone reached more than 90%, while the pore water was mainly distributed in coexistence zone. Thus, the phase saturation (gas phase, water phase, and hydrate phase) in coexistence area was analyzed, as shown in Fig. 10. The hydrate saturation increased form 35% before the gas-water migration to more than 51.6% in hydrate seal, indicating that the hydrate reformed during the gas-water migration process was the development mechanism of hydrate seal. In addition, Zhao et al. (2022b) had found that sufficient pore water was an indispensable factor for the formation of hydrate seal. In addition, the pore water produced larger capillary pressure due to the reduction on the effective radii of the pore throats caused by hydrate formation. There were bright areas of Cases 3–7 existed in MRI images, indicating pore water existed in the pore space of hydrate seal. In this study, the water saturation was more than 19.3% when the overpressure of hydrate seal reached more than 9.0 MPa.

4. Conclusion

In this study, the gas-water migration at 274.15 K, 3.5 or 4.0 MPa in hydrate-bearing sediments was investigated using an MRI visualization device. The results are summarized as follows:

(1) Low gas-water flow rate (1–0.25 mL/min) at low reservoir pressure (3.5 MPa) or high gas-water flow rate (2–0.5 and 4–1 mL/min) at high reservoir pressure (4.0 MPa) induced

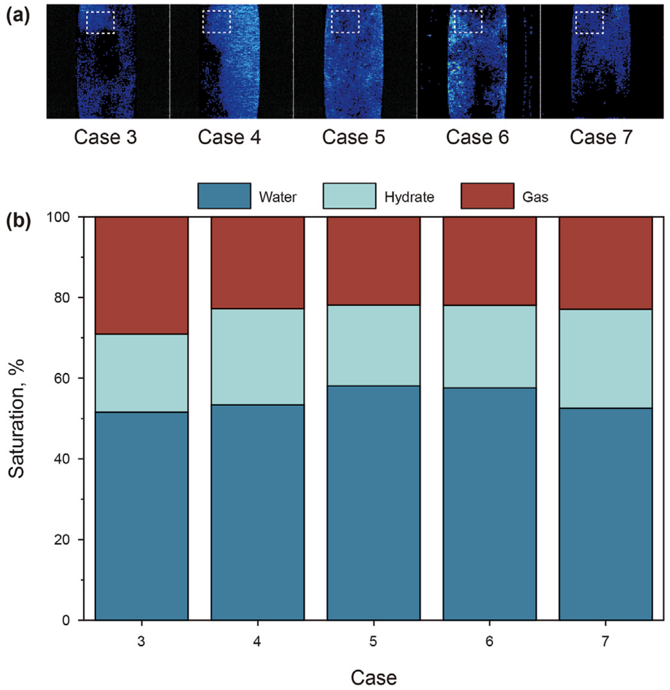

Fig. 10. State of hydrate seal with high overpressure zone: (**a**) the reference areas in MRI images; (**b**) phase saturation.

hydrate reformation in hydrate-bearing sediment. Hydrate reformation is the development mechanism of hydrate seal.

(2) The hydrate saturation of hydrate seal was more than 51.6%, and the water saturation was more than 19.3%. The overpressure of at least 9.0 MPa can exist stable below the hydrate seal. This overpressure provides the development condition for the gas and/or water layer beneath the hydrate layer in marine sediments.

(3) A composite MRI image of hydrate seal was demonstrated through MRI. The pore difference between hydrate zone and coexistence zone was visually observed, which contributes to the capillary sealing effect of hydrate-bearing sediment. The hydrate zone and coexistence zone were formed and distributed vertically along the migration direction.

(4) The hydrate seal could be broken through when the overpressure exceeded the capillary pressure and caused a sudden drop in reservoir pressure. This phenomenon should be considered during the exploitation process of gas hydrate with underlying gas reservoirs.

Declaration of competing interest

The authors declare that they have no known competing financial interests or personal relationships that could have appeared to influence the work reported in this paper.

Acknowledgments

This project was financially supported by the National Key Research and Development Plan of China (2021YFC2800902), the National Natural Science Foundation of China (52206076, U19B2005), the Fundamental Research Funds for the Central Universities of China (DUT21ZD103) and the Opening Fund of MOE Key Laboratory of Ocean Energy Utilization and Energy Conservation (LOEC-202204).

Appendix A. Supplementary data

Supplementary data to this article can be found online at https://doi.org/10.1016/j.petsci.2023.07.017.

References

Almenningen, S., Gauteplass, J., Fotland, P., et al., 2018. Visualization of hydrate formation during CO_2 storage in water-saturated sandstone. Int. J. Greenh. Gas Control 119, 678–687. https://doi.org/10.1016/j.ijggc.2018.11.008.

Behseresht, J., Bryant, S.L., 2017. Physical mechanisms for multiphase flow associated with hydrate formation. J. Geophys. Res. Solid Earth 122 (5), 3585–3623. https://doi.org/10.1002/2016JB013503.

Bello-Palacios, A., Fotland, P., Almenningen, S., et al., 2022. Effects of methane hydrates on two-phase relative permeability in sandstone: numerical simulation of laboratory experiments. J. Petrol. Sci. Eng. 208, 109606. https://doi.org/10.1016/j.petrol.2021.109606.

Buleiko, V.M., Grigoriev, B.A., Istomin, V.A., 2017. Capillary effects on phase behavior of liquid and gaseous propane and dynamics of hydrate formation and dissociation in porous media. Fluid Phase Equil. 441, 64–71. https://doi.org/10.1016/j.fluid.2017.01.026.

Bünz, S., Mienert, J., Berndt, C., 2003. Geological controls on the Storegga gas-hydrate system of the mid-Norwegian continental margin. Earth Planet Sci. Lett. 209 (3-4), 291–307. https://doi.org/10.1016/S0012-821X(03)00097-9.

Cathles, L.M., 2007. Changes in sub-water table fluid flow at the end of the Proterozoic and its implications for gas pulsars and MVT lead-zinc deposits. Geofluids 7 (2), 209–226. https://doi.org/10.1111/j.1468-8123.2007.00176.x.

Chatterjee, S., Bhatnagar, G., Dugan, B., et al., 2014. The impact of lithologic heterogeneity and focused fluid flow upon gas hydrate distribution in marine sediments. J. Geophys. Res. Solid Earth 119 (9), 6705–6732. https://doi.org/10.1002/2014JB011236.

Chen, B., Sun, H., Li, K., et al., 2019. Experimental investigation of natural gas hydrate production characteristics via novel combination modes of depressurization with water flow erosion. Fuel 252, 295–303. https://doi.org/10.1016/j.fuel.2019.04.120.

Chen, B.B., Sun, H.R., Zheng, J.J., et al., 2020. New insights on water-gas flow and hydrate decomposition behaviors in natural gas hydrates deposits with various saturations. Appl. Energy. 259, 114185. https://doi.org/10.1016/j.apenergy.2019.114185.

Chong, Z.R., Yin, Z., Tan, J., et al., 2017. Experimental investigations on energy recovery from water-saturated hydrate bearing sediments via depressurization approach. Appl. Energy. 204, 1513–1525. https://doi.org/10.1016/j.apenergy.2017.04.031.

Clennell, M.B., Henry, P., Hovland, M., et al., 1999. Formation of natural gas hydrates in marine sediments: 1. Conceptual model of gas hydrate growth conditioned by host sediment properties. Ann. N. Y. Acad. Sci. 104 (1), 22985–23003. https://doi.org/10.1029/1999JB900175.

Collett, T., Bahk, J.J., Baker, R., et al., 2015. Methane hydrates in nature-current knowledge and challenges. J. Chem. Eng. Data. 60 (2), 319–329. https://doi.org/10.1021/je500604h.

Davie, M.K., Buffett, B.A., 2003. Sources of methane for marine gas hydrate: inferences from a comparison of observations and numerical models. Earth Planet Sci. Lett. 206 (1-2), 51–63. https://doi.org/10.1016/S0012-821X(02)01064-6.

De La Fuente, M., Vaunat, J., Marin-Moreno, H., 2021. Modelling methane hydrate saturation in pores: capillary inhibition effects. Energies 14 (18), 5627. https://doi.org/10.3390/en14185627.

Dong, S., Yang, M.J., Chen, M.K., et al., 2022. Thermodynamics analysis and temperature response mechanism during methane hydrate production by depressurization. Energy 241, 122902. https://doi.org/10.1016/j.energy.2021.122902.

Hou, J., Ji, Y.K., Zhou, K., et al., 2018. Effect of hydrate on permeability in porous media: pore-scale micro-simulation. Int. J. Heat Mass Tran. 126, 416–424. https://doi.org/10.1016/j.ijheatmasstransfer.2018.05.156.

Huang, J.W., Bellefleur, G., Milkereit, B., 2009. Seismic modeling of multidimensional heterogeneity scales of Mallik gas hydrate reservoirs, Northwest Territories of Canada. J. Geophys. Res. Solid Earth 114, B07306. https://doi.org/10.1029/2008JB006172.

Kagan, M., Pinczewski, W.V., 2000. Menisci in a diamond-shaped capillary. J. Colloid Interface Sci. 230 (2), 452–454. https://doi.org/10.1006/jcis.2000.7077.

Kang, Q., Song, S.F., Yu, J.H., et al., 2021. Simulation of upward gas-hydrate slurry multiphase flow in a vertical concentric annulus for natural gas hydrate solid fluidization exploitation. Phys. Fluids 33 (10), 103102. https://doi.org/10.1063/5.0062704.

Kannberg, P.K., Trehu, A.M., Pierce, S.D., et al., 2013. Temporal variation of methane flares in the ocean above Hydrate Ridge, Oregon. Earth Planet Sci. Lett. 368, 33–42. https://doi.org/10.1016/j.epsl.2013.02.030.

Kleinberg, R.L., Flaum, C., Griffin, D.D., 2003. Deep sea NMR: methane hydrate growth habit in porous media and its relationship to hydraulic permeability, deposit accumulation, and submarine slope stability. J. Geophys. Res. Solid Earth 108 (B10), 2508. https://doi.org/10.1029/2003JB002389.

Konno, Y., Fujii, T., Sato, A., et al., 2017. Key findings of the world's first offshore methane hydrate production test off the coast of Japan: toward future commercial production. Energy Fuels 31 (3), 2607–2616. https://doi.org/10.1021/acs.energyfuels.6b03143.

Li, X.S., Xu, C.G., Zhang, Y., et al., 2016. Investigation into gas production from natural gas hydrate: a review. Appl. Energy. 172, 286–322. https://doi.org/10.1016/j.apenergy.2016.03.101.

Liu, X.L., Flemings, P.B., 2006. Passing gas through the hydrate stability zone at southern Hydrate Ridge, offshore Oregon. Earth Planet Sci. Lett. 241 (1-2), 211–226. https://doi.org/10.1016/j.epsl.2005.10.026.

Liu, L.P., Sun, Z.L., Zhang, L., et al., 2019a. Progress in global gas hydrate development and production as a new energy resource. Acta Geol. Sin. 93 (3), 231–255. https://doi.org/10.1111/1755-6724.13876.

Liu, J.L., Haeckel, M., Rutqvist, J., et al., 2019b. The mechanism of methane gas migration through the gas hydrate stability zone: insights from numerical simulations. J. Geophys. Res. Solid Earth 124 (5), 4399–4427. https://doi.org/10.1029/2019JB017417.

Liu, W., Wu, Z.R., Li, Y.H., et al., 2016. Experimental study on the gas phase permeability of methane hydrate-bearing clayey sediments. J. Nat. Gas Sci. Eng. 36 (Part A), 378–384. https://doi.org/10.1016/j.jngse.2016.10.055.

Lpa, B., Ksa, B., Akj, A., 2019. Estimate of gas hydrate saturations in the Krishna-Godavari basin, eastern continental margin of India, results of expedition NGHP-02. Mar. Petrol. Geol. 108, 581–594. https://doi.org/10.1016/j.marpetgeo.2018.12.009.

Ma, S., Zheng, J.N., Tian, M., et al., 2020. NMR quantitative investigation on methane hydrate formation characteristics under different driving forces. Fuel 261, 116364. https://doi.org/10.1016/j.fuel.2019.116364.

Makogon, Y.F., Holditch, S.A., Makogon, T.Y., 2007. Natural gas-hydrates - a potential energy source for the 21st Century. J. Petrol. Sci. Eng. 56 (1-3), 14–31. https://doi.org/10.1016/j.petrol.2005.10.009.

Meazell, K., Flemings, P.B., 2022. The evolution of seafloor venting from hydrate-sealed gas reservoirs. Earth Planet Sci. Lett. 579, 117336. https://doi.org/10.1016/j.epsl.2021.117336.

Moridis, G.J., Collett, T.S., Boswell, R., et al., 2009. Toward production from gas hydrates: current status, assessment of resources, and simulation-based evaluation of technology and potential. SPE Reservoir Eval. Eng. 12 (5), 745–771. https://doi.org/10.2118/114163-PA.

Nakayama, T., Matsumoto, M., Tanaka, H., 2013. On the thermodynamic stability of hydrogen hydrates in the presence of promoter molecules. Solar Thermochemical Energy Storage 1568, 46–52. https://doi.org/10.1063/1.4848090.

Peng, Y., Liu, W., Sun, X., et al., 2019. A microfocus x-ray computed tomography based gas hydrate triaxial testing apparatus. Rev. Sci. Instrum. 90 (5), 55106. https://doi.org/10.1063/1.5095812.

Pohlman, J.W., Kaneko, M., Heuer, V.B., et al., 2009. Methane sources and production in the northern Cascadia margin gas hydrate system. Earth Planet Sci. Lett. 287 (3-4), 504–512. https://doi.org/10.1016/j.epsl.2009.08.037.

Qin, X.W., Lu, J.A., Lu, H.L., et al., 2020. Coexistence of natural gas hydrate, free gas and water in the gas hydrate system in the Shenhu Area, South China Sea. China Geology 3 (2), 210–220. https://doi.org/10.31035/cg2020038.

Riedel, M., Collett, T.S., 2017. Observed correlation between the depth to base and top of gas hydrate occurrence from review of global drilling data. G-cubed 18 (7), 2543–2561. https://doi.org/10.1002/2017GC006805.

Sadeq, D., Alef, K., Iglauer, S., et al., 2018a. Compressional wave velocity of hydrate-bearing bentheimer sediments with varying pore fillings. Int. J. Hydrogen Energy 43 (52), 23193–23200. https://doi.org/10.1016/j.ijhydene.2018.10.169.

Sadeq, D., Iglauer, S., Lebedev, M., et al., 2018b. Prediction of hydrate phase equilibrium conditions for different gas mixtures. Offshore Technology Conference Asia. https://doi.org/10.4043/28478-MS.

Sadeq, D., Iglauer, S., Lebedev, M., et al., 2018c. Experimental pore-scale analysis of carbon dioxide hydrate in sandstone via X-Ray micro-computed tomography. Int. J. Greenh. Gas Control 79, 73–82. https://doi.org/10.1016/j.ijggc.2018.10.006.

Sadeq, D., Iglauer, S., Lebedev, M., et al., 2017. Experimental determination of hydrate phase equilibrium for different gas mixtures containing methane, carbon dioxide and nitrogen with motor current measurements. J. Nat. Gas Sci. Eng. 38, 59–73. https://doi.org/10.1016/j.jngse.2016.12.025.

Seol, Y., Kneafsey, T.J., 2011. Methane hydrate induced permeability modification for multiphase flow in unsaturated porous media. J. Geophys. Res. Solid Earth. 116, B08102. https://doi.org/10.1029/2010JB008040.

Shen, X.D., Hou, G.D., Ding, J.X., et al., 2018. Flow characteristics of methane hydrate slurry in the transition region in a high-pressure flow loop. J. Nat. Gas Sci. Eng. 55, 64–73. https://doi.org/10.1016/j.jngse.2018.04.023.

Smith, A.J., Flemings, P.B., Liu, X.L., et al., 2014. The evolution of methane vents that pierce the hydrate stability zone in the world's oceans. J. Geophys. Res. Solid Earth. 119 (8), 6337–6356. https://doi.org/10.1002/2013JB010686.

Song, Y., Wang, P., Jiang, L., et al., 2015. Methane hydrate formation/reformation in three experimental modes: a preliminary investigation of blockage prevention during exploitation. J. Nat. Gas Sci. Eng. 27, 1814–1820. https://doi.org/10.1016/j.jngse.2015.11.009.

Su, Z., Cao, Y.C., Wu, N.Y., et al., 2009. Numerical computation and case analysis of the venting process of free gas beneath hydrate layer. Chin. J. Geophys. 52 (12), 3124–3131. https://doi.org/10.3969/j.issn.0001-5733.2009.12.022.

Sun, H., Chen, B., Zhao, G., et al., 2020a. Utilization of water-gas flow on natural gas hydrate recovery with different depressurization modes. Fuel 288 (15), 119583. https://doi.org/10.1016/j.fuel.2020.119583.

Sun, H., Chen, B.B., Zhao, G.J., et al., 2020b. The enhancement effect of water-gas two-phase flow on depressurization process: important for gas hydrate production. Appl. Energy 276, 115559. https://doi.org/10.1016/j.apenergy.2020.115559.

Torres, M.E., Wallmann, K., Trehu, A.M., et al., 2004. Gas hydrate growth, methane transport, and chloride enrichment at the southern summit of Hydrate Ridge, Cascadia margin off Oregon. Earth Planet Sci. Lett. 226 (1-2), 225–241. https://doi.org/10.1016/j.epsl.2004.07.029.

Touil, A., Broseta, D., Desmedt, A., 2019. Gas hydrate crystallization in thin glass capillaries: roles of supercooling and wettability. Langmuir 35 (38), 12569–12581. https://doi.org/10.1021/acs.langmuir.9b01146.

Vangenuchten, M.T., 1980. A closed-form equation for predicting the hydraulic conductivity of unsaturated soils. Soil Science Society of America 44 (5), 892–898. https://doi.org/10.2136/sssaj1980.03615995004400050002x.

Wang, P., Wang, S., Song, Y., et al., 2017. Methane hydrate formation and decomposition properties during gas migration in porous medium. Energy Proc. 105, 4668–4673. https://doi.org/10.1016/j.egypro.2017.03.1012.

Wang, S., Liu, Y., Zhao, Y., et al., 2020. Enhanced mass transfer by density-driven convection during CO_2 geological storage. Ind. Eng. Chem. Res. 59 (19), 9300–9309. https://doi.org/10.1021/acs.iecr.0c00525.

Wang, Z.Y., Liao, Y.Q., Zhang, W.D., et al., 2018. Coupled temperature field model of gas-hydrate formation for thermal fluid fracturing. Appl. Therm. Eng. 133, 160–169. https://doi.org/10.1016/j.applthermaleng.2018.01.039.

Xu, W., Ruppel, C., 1999. Predicting the occurrence, distribution, and evolution of methane gas hydrate in porous marine sediments. J. Geophys. Res. Solid Earth 104 (B3), 5081–5096. https://doi.org/10.1029/1998JB900092.

Yang, M.J., Sun, H., Chen, B., et al., 2019. Effects of water-gas two-phase flow on methane hydrate dissociation in porous media. Fuel 255, 115637. https://doi.org/10.1016/j.fuel.2019.115637.

Yang, L., Ai, L., Xue, K.H., et al., 2018. Analyzing the effects of inhomogeneity on the permeability of porous media containing methane hydrates through pore network models combined with CT observation. Energy 163, 27–37. https://doi.org/10.1016/j.energy.2018.08.100.

Yang, L., Wang, J., Jiang, Y., 2020. Experimental study and numerical simulation of overlying layer soil failure caused by hydrate decomposition. ACS Omega 5 (48), 31244–31253. https://doi.org/10.1021/acsomega.0c04619.

Yang, M., Zhao, G.J., Sun, H.R., et al., 2022. In-situ investigation on methane hydrate decomposition characteristics under variational seawater flow process. Fuel 310, 122123. https://doi.org/10.1016/j.fuel.2021.122123.

Yang, M.J., Song, Y.C., Zhao, Y.C., et al., 2011. MRI measurements of CO_2 hydrate dissociation rate in a porous medium. Magn. Reson. Imag. 29 (7), 1007–1013. https://doi.org/10.1016/j.mri.2011.04.008.

You, K.H., DiCarlo, D., Flemings, P.B., 2015. Quantifying hydrate solidification front advancing using method of characteristics. J. Geophys. Res. Solid Earth 120 (10), 6681–6697. https://doi.org/10.1002/2015JB011985.

Yu, T., Guan, G., Abudula, A., et al., 2019. Application of horizontal wells to the oceanic methane hydrate production in the Nankai Trough, Japan. J. Nat. Gas Sci. Eng. 62, 113–131. https://doi.org/10.1016/j.jngse.2018.11.027.

Yuan, Y.L., Xu, T.F., Xin, X., et al., 2017. Multiphase flow behavior of layered methane hydrate reservoir induced by gas production. Geofluids, 7851031. https://doi.org/10.1155/2017/7851031.

Zhang, L., Sun, L., Sun, M., et al., 2019. Analyzing spatially and temporally visualized formation behavior of methane hydrate in unconsolidated porous media. Magn. Reson. Imag. 61, 224–230. https://doi.org/10.1016/j.mri.2019.06.005.

Zhang, L.X., Sun, M.R., Sun, L.J., et al., 2020. In-situ observation for natural gas hydrate in porous medium: water performance and formation characteristic. Magn. Reson. Imag. 65, 166–174. https://doi.org/10.1016/j.mri.2019.09.002.

Zhang, Y.C., Liu, L.L., Hu, G.W., et al., 2022. Formation mechanism, experimental method, and property characterization of grain-displacing methane hydrates in marine sediment: a review. China Geology 5 (2), 345–354. https://doi.org/10.31035/cg2022014.

Zhao, G., Gong, G.J., Sun, H.R., et al., 2022a. Effect of methane solubility on hydrate formation and dissociation: review and perspectives. Energy Fuels 36 (14), 7269–7283. https://doi.org/10.1021/acs.energyfuels.2c01017.

Zhao, G., Yang, M.J., Pang, W.X., et al., 2022b. Effects of hydrate cap on leakage prevention and capacity improvement of sub-seabed CO_2 sequestration. Chem. Eng. J. 450, 138493. https://doi.org/10.1016/j.cej.2022.138493.

Zhao, J., Zheng, J.N., Wang, X.R., et al., 2022c. Effects of underlying gas on formation and gas production of methane hydrate in muddy low-permeability cores. Fuel 309, 122128. https://doi.org/10.1016/j.fuel.2021.122128.